Plasma Sources Science and Technology

Check for updates

OPEN ACCESS

RECEIVED
23 January 2026

REVISED
24 March 2026

ACCEPTED FOR PUBLICATION
10 April 2026

PUBLISHED
29 April 2026

Original content from this work may be used under the terms of the Creative Commons Attribution 4.0 licence.

Any further distribution of this work must maintain attribution to the author(s) and the title of the work, journal citation and DOI.

PAPER

# Magnetically induced formation and disruption of striations in capacitively coupled radio-frequency $CF_4$ plasmas

**Li Wang[1,*], Aranka Derzsi[2], Peter Hartmann[2], Zoltán Donkó[2], Maximilian Ryppa[1], Constantin Neuroth[1], Florian Beckfeld[1], Wan Dong[1,3], Yuan-Hong Song[3] and Julian Schulze[1]**

[1] Chair of Applied Electrodynamics and Plasma Technology, Department of Electrical Engineering and Information Technology, Ruhr University Bochum, Bochum D-44780, Germany
[2] Institute for Solid State Physics and Optics, HUN-REN Wigner Research Centre for Physics, H-1121 Budapest, Konkoly-Thege Miklós str. 29-33, Hungary
[3] Key Laboratory of Materials Modification by Laser, Ion, and Electron Beams (Ministry of Education), School of Physics, Dalian University of Technology, Dalian 116024, People's Republic of China
[*] Author to whom any correspondence should be addressed.

**E-mail:** wang@aept.rub.de

**Keywords:** striation mode, PIC/MCC simulation, magnetized CCPs, magnetized drift-ambipolar mode, electronegative $CF_4$ plasmas

## Abstract

The influence of externally applied homogeneous transverse magnetic fields of up to 200 G on self-organized striations in capacitively coupled radio-frequency (RF) $CF_4$ plasmas is investigated using kinetic simulations. The striations are known to originate from a resonance between the applied RF excitation and the eigenfrequency of the ion–ion plasma, the magnetic field is found to affect the striations indirectly through its impact on electron dynamics as ions do not get magnetized within the range of magnetic fields covered. Depending on the discharge conditions, increasing the magnetic field can either switch striations on or off and, in this way, strongly affect the spatial electron energy distribution function as well as the generation of process relevant charged and neutral species. We demonstrate that at some discharge conditions where striations form in the absence of a magnetic field, applying a moderate B-field can lead to the suppression of striations near the discharge center as a result of enhanced electron power absorption and a corresponding increase in electron density, enabling electrons to neutralize the space charge caused by the ion oscillations. We also illustrate the opposite effect that can occur at some other operating conditions, where the plasma operates close to the striation regime, but striations are absent due to insufficient ion densities, the magnetic field enhances the ion density and amplifies the local space charge formation, which can no longer be balanced by electrons. As a result, striations appear, inducing a transition from the drift ambipolar to a striation/magnetized drift ambipolar hybrid mode.

## 1. Introduction

Capacitively coupled plasmas (CCPs) are extensively used in microelectronics manufacturing for processes such as surface etching, thin-film deposition, and sputtering, owing to their structurally simple reactor configurations and their capability to sustain large-area plasmas with excellent radial uniformity [1–3]. These plasma-assisted processes, however, impose strict requirements on the precise control of fundamental plasma parameters, including charged particle densities, their flux-energy distribution functions, as well as the production rates of reactive radical species [4–9]. Electron power absorption, as one of the most fundamental mechanisms in CCPs, governs the conversion of externally applied power into plasma generation and sustainment and shapes the electron energy distribution function, thereby playing a key role in determining these process relevant plasma parameters [10–15].

Based on previous studies, several typical CCP operation modes, distinguished by their unique spatio-temporal electron power absorption dynamics, have been identified. Specifically, the $\alpha$-mode [16, 17] is characterized by pronounced electron power absorption and ionization near the expanding sheath edges, which, in recent years, has been explained in detail by ambipolar electric field heating based on a

© 2026 The Author(s). Published by IOP Publishing Ltd

Boltzmann term analysis [17–19]. The $\gamma$-mode is dominated by the power absorption of secondary electrons emitted from the electrode surfaces, which gain substantial amounts of energy within the sheaths, and their collisional multiplications inside the sheaths. This mode typically occurs under high-pressure and high-voltage operating conditions [16, 20, 21]. In electronegative plasmas, a strong drift electric field, resulting from the low electron density and conductivity in the plasma bulk, and a strong ambipolar electric field, arising from the steep electron density gradient in the electropositive edge regions, can develop within the bulk and near the collapsing sheath edges, respectively. The mode in which these fields contribute significantly to the electron power absorption is known as the drift-ambipolar (DA) mode [22]. Mode transitions from the $\alpha$-mode to the DA mode have been reported to be induced by variations in the external driving power [23, 24]. Moreover, in electronegative CCPs, energetic electrons can be produced by the formation of negative ions close to the electrodes during the local sheath collapse via electron attachment and the subsequent acceleration of such negative ions towards the plasma bulk by the sheath electric field. Inside the sheath, electrons can then be detached from the negative ions and gain substantial amounts of energy by acceleration via the sheath electric field. This mode is called detachment induced (DI) mode [25, 26].

In addition to the operation modes mentioned above, the striation (STR) mode is another commonly observed CCP operation mode under strongly electronegative conditions, e.g. in $CF_4$ discharges [27–30]. Both experiments and simulations have shown that, if the plasma density is sufficiently high so that the ion plasma frequency is comparable to the radio-frequency (RF) driving frequency, striated patterns emerge in the spatio-temporal electric field, electron power absorption, as well as ionization rate. This phenomenon was explained based on an ion–ion plasma model (with electrons neglected), where the formation of striations is attributed to the resonance between the external RF driving frequency and the eigenfrequency of the ion–ion plasma. Based on this resonance condition, a critical ion density beyond which striations can be formed has been derived: $n_{\mathrm{critical}} = \omega_{\mathrm{rf}}^2 \varepsilon_0 \mu / e^2$, where $\omega_{\mathrm{rf}}$ is the angular frequency of the external driving voltage, $\varepsilon_0$ is the permittivity in vacuum, $\mu$ is the reduced mass of the positive and negative ions, and $e$ is the elementary charge [27, 31]. Kinetic simulations were also conducted intensively for understanding the underlying mechanisms. Once the ion density exceeds the critical value, positive and negative ions start to oscillate with small amplitudes in opposite directions under the RF field, thereby generating spatially alternating space charges and an associated internal electric field. This internal field locally enhances or diminishes the external field, producing the characteristic striated patterns in the spatio-temporal distributions of the electric field and other relevant plasma parameters. The electron power absorption mechanisms in the striation regime were studied in detail based on the Boltzmann term analysis [30, 32]. In addition, further studies on the effects of external control parameters, including the driving frequency, voltage amplitude, voltage waveform, gas pressure, gap distance, and secondary electron emission, on the formation and characteristics of the striations have also been performed in various electronegative discharges, i.e. $CF_4$, $O_2$, and $Cl_2$ [28–30, 33–35].

The influence of external magnetic fields on the striations has never been addressed, although magnetized CCPs are extensively used in RF magnetron sputtering and magnetically enhanced reactive etching due to their effectiveness in controlling key plasma properties, particularly the plasma density [36–43]. Previous studies have revealed that, when a static magnetic field of tens to hundreds of Gauss is applied to the plasma, the electron power absorption dynamics is substantially altered [44–50]. For instance, applying a transversal magnetic field to the discharge is found to induce a transition from a pressure-heating dominated mode to an Ohmic-heating dominated mode [51]. In oxygen discharges, such an external magnetic field can strongly reduce the plasma electronegativity and thereby trigger a DA to $\alpha$-mode transition [52, 53]. Electric field reversals during the sheath collapse phase have also been reported to be induced by an external magnetic field, which can significantly contribute to the electron power absorption [38, 52]. In addition, the magnetic asymmetry effect (MAE), which arises in plasmas exposed to non-uniform magnetic fields and enables control of the DC self-bias and the ion energy distribution function (IEDF) by adjusting the B-field, has also been investigated in detail [54–59].

In strongly electronegative $CF_4$ plasmas, striations will generally emerge if the ion density exceeds the critical threshold. However, under conditions where the ion density remains well below this threshold and the discharge operates in the DA mode, the application of an external magnetic field has been shown to induce the formation of electropositive regions, i.e. pronounced electron density peaks embedded within an otherwise electronegative plasma bulk, referred to as the magnetized DA (m-DA) mode [60]. Such electron density peaks are generated, because a large number of low-energy electrons are produced through strong ionization at specific locations within the plasma bulk, where electrons have

gained sufficient energy from the drift electric field. These low-energy electrons are then locally confined by the magnetic field, which enhances the local conductivity and significantly reduces the electric field. As a result, the electrons can hardly be further accelerated, leading to the formation of localized electron density peaks. In these discharges, electrons are magnetized whereas ions remain essentially unmagnetized. This raises an important question: can an externally applied magnetic field influence the formation of striations, which rely on the resonance between the RF driving frequency and the eigenfrequency of the ion–ion plasma? In this work, we investigate the effects of such an external magnetic field on $CF_4$ plasmas operated in or near the striation regime, i.e. when the ion density is well above or around the critical value. While our previous work [60] focused on the formation mechanism of magnetically induced electron density peaks in the m-DA mode and magnetically induced transitions from the DA- into the m-DA-mode in the absence of striations, the present work investigates the influence of an external magnetic field on the striation mode in electronegative $CF_4$ plasmas. In particular, we show that the magnetic field can significantly modify the striation structure in two opposite ways: (1) the suppression of existing striations and (2) the formation of new striations under otherwise non-striated discharge conditions. These effects highlight the important role of electron dynamics in the formation and control of striations in electronegative CCPs. These magnetically induced modifications of the discharge mode also lead to substantial changes in production of radicals, which is highly relevant for industrial applications.

The paper is structured as follows: section 2 describes the simulation method applied in this work. The results are presented in section 3, which is divided into two parts: magnetic field induced disruption of striations (section 3.1) and magnetic field induced formation of striations (section 3.2). Finally, conclusions are drawn in section 4.

## 2. Computational method

The simulations performed in this work are based on a one dimensional in space and three dimensional in velocity space (1d3v) particle in cell/Monte Carlo collision (PIC/MCC) code, named PICit! [62]. This code is able to simulate geometrically symmetric CCPs of various gases and gas mixtures. The $CF_4$ component of PICit! extends the previously developed $CF_4$ code, which has been validated against experimental data through comparisons of the DC self-bias and the spatio-temporal electron dynamics with phase-resolved optical emission spectroscopy measurements [27, 31, 63]. The extension of the code was done by incorporating additional species. Specifically, in addition to $CF_3^+$, $CF_3^-$, $F^-$ ions considered in the prior code [63], four new ion species, i.e. $CF_2^+$, $CF^+$, $C^+$, and $F^+$, are added and traced in the simulations. Besides that, 6 different neutral species, i.e. $CF_3$, $CF_2$, CF, C, F, $F_2$, are also included and their density distributions are calculated self-consistently. These species are incorporated considering their importance in industrial applications. To calculate the densities of these particles self-consistently, new ion-molecule reactions are included. The $e^- + CF_4$ collisions considered in the simulations (17 processes) are listed in table 1 and are kept the same as in the prior model. The electron impact cross section set is based on the work of Kurihara *et al* [61]. This cross section set includes only one electron attachment process, to form $F^-$ (process 13). In order to consider the formation of $CF_3^-$ negative ions as well (process 14), both dissociative attachment cross sections (processes 13 and 14) are taken from the work of Bonham [64]. The (positive/negative) ions created in these processes are traced in the simulations, except the doubly-charged ions, i.e. $CF_3^{++}$ and $CF_2^{++}$ (from processes 6 and 8). While these ions are not traced in the simulations, their effects on the electron kinetics are taken into account via the corresponding losses of the electron's kinetic energy. Figure 1(a) shows the cross sections of the electron reactions included in the model.

In $CF_4$ plasmas, ion-molecule reactions can proceed via a wide range of channels [65, 67, 68]. The ion-molecule reaction sets in our model are extended based on the work of Kazuki Denpoh [66, 69]. Examples of the (positive/negative) ion + $CF_4$ molecule collision processes are listed in table 2, while the full lists of the ion + $CF_4$ molecule collision processes can be found in [66, 69]. For each ion species, ten collision processes with the lowest energy thresholds are shown in table 2. These collisions can be both of elastic and reactive nature. For elastic ion-molecule interactions, a Langevin-type cross section is used. Both isotropic and anisotropic angular scattering are considered, depending on the randomly sampled impact parameter. In reactive collisions, the type of the incoming ion may either be preserved or changed as a consequence of the interaction between the projectile and the target ($CF_4$ molecule) species. The cross sections of the exemplary collision processes listed in table 2 are plotted in figures 1(b)–(h). The rate coefficients for ion–ion recombination are taken from [70], and for electron–ion recombination from [71].

**Table 1.** List of $e^- + CF_4$ collision processes considered in the model. $\Delta E$ is the energy threshold in eV. The cross section set is based on [61].

| # | Process | Collision type | $\Delta E$ |
|---|---|---|---|
| 1 | $e^- + CF_4 \longrightarrow e^- + CF_4$ | Elastic scattering | 0 |
| 2 | $e^- + CF_4 \longrightarrow e^- + CF_4(v=1)$ | Vibrational excitation | 0.108 |
| 3 | $e^- + CF_4 \longrightarrow e^- + CF_4(v=3)$ | Vibrational excitation | 0.168 |
| 4 | $e^- + CF_4 \longrightarrow e^- + CF_4(v=4)$ | Vibrational excitation | 0.077 |
| 5 | $e^- + CF_4 \longrightarrow e^- + CF_4^*$ | Electronic excitation | 7.54 |
| 6 | $e^- + CF_4 \longrightarrow 3e^- + CF_3^{++} + F$ | Dissociative ionization | 41 |
| 7 | $e^- + CF_4 \longrightarrow 2e^- + CF_3^{+} + F$ | Dissociative ionization | 16 |
| 8 | $e^- + CF_4 \longrightarrow 3e^- + CF_2^{++} + 2F$ | Dissociative ionization | 42 |
| 9 | $e^- + CF_4 \longrightarrow 2e^- + CF_2^{+} + 2F$ | Dissociative ionization | 21 |
| 10 | $e^- + CF_4 \longrightarrow 2e^- + CF^{+} + 3F$ | Dissociative ionization | 26 |
| 11 | $e^- + CF_4 \longrightarrow 2e^- + C^{+} + 4F$ | Dissociative ionization | 34 |
| 12 | $e^- + CF_4 \longrightarrow 2e^- + F^{+} + CF_3$ | Dissociative ionization | 34 |
| 13 | $e^- + CF_4 \longrightarrow F^- + CF_3$ | Dissociative attachment | 5 |
| 14 | $e^- + CF_4 \longrightarrow CF_3^- + F$ | Dissociative attachment | 5 |
| 15 | $e^- + CF_4 \longrightarrow e^- + CF_3 + F$ | Neutral dissociation | 12 |
| 16 | $e^- + CF_4 \longrightarrow e^- + CF_2 + 2F$ | Neutral dissociation | 17 |
| 17 | $e^- + CF_4 \longrightarrow e^- + CF + 3F$ | Neutral dissociation | 18 |

The densities of radical species ($CF_3$, $CF_2$, CF, C, F) and $F_2$ are determined self-consistently by modeling the balance of creation, transport, and surface loss. This method has been described in detail in a previous work on neon–oxygen discharges conducted by the PICit! code [62]. In this method, the pressure and temperature dependent diffusion coefficients are calculated based on the predictions of the Chapman–Enskog theory [72, 73]:

$$D \approx D_0 \frac{p_0}{p} \left( \frac{T_{\mathrm{gas}}}{T_0} \right)^{3/2}, \tag{1}$$

where $D_0$ is the diffusion coefficient at a reference pressure $p_0 = 1$ Pa and reference temperature $T_0 = 300$ K. The values of $D_0$ for the various neutral species are calculated as in reference [74]:

$$D_0 = \frac{1.86 \times 10^{-3}\ T_0^{3/2} \left(1/M_{\mathrm{R}} + 1/M_{\mathrm{CF_4}}\right)^{1/2}}{\left(p_0/101325\right) \sigma_{12}^2 \Omega}, \tag{2}$$

where $M_{\mathrm{R}}$ and $M_{\mathrm{CF_4}}$ are the molecular weights of a given neutral species ($CF_3$, $CF_2$, CF, C, $F_2$, F) and $CF_4$. The collision diameter $\sigma_{12} = \left(\sigma_{\mathrm{R}} + \sigma_{\mathrm{CF_4}}\right)/2$ is the arithmetic average of the Lennard–Jones collision cross section (given in Angstroms) of the two species. For $CF_4$ and the other neutral species, these parameters are taken from table III of [75]. The dimensionless quantity, $\Omega$, is determined by the depth of the Lennard–Jones potential well of the interacting species. The energy of interaction, $\varepsilon_{12} = \sqrt{\varepsilon_{\mathrm{R}} \varepsilon_{\mathrm{CF_4}}}$, is a geometric average of contributions from the two species. Values of $\varepsilon/k_{\mathrm{B}}$ are also given in table III of [75]. Once $\varepsilon_{12}$ is known, $\Omega$ can be found as a function of $k_{\mathrm{B}}T/\varepsilon_{12}$ based on the values in tables 5.1–3 in [74] by linear interpolation. The values of $D_0$ for the radical species and $F_2$ are included in table 3.

In our model, due to the lack of various surface process rate coefficients, the surface interactions of each radical species and $F_2$ are treated using a constant surface loss probability. This effective parameter accounts for the net loss of particles at the surfaces, including adsorption, recombination, and other surface reactions, without explicitly resolving individual processes. This approach provides a simplified but physically reasonable description of surface effects under the relatively high-pressure conditions studied here [76]. The surface loss probabilities of the radical species and $F_2$ considered in this work are summarized in table 4, which are taken from [76] (for $CF_3$, $CF_2$, CF, and C), and from [77, 78] (for F), and have been previously applied in simulations assuming stainless steel surfaces. For $F_2$, no reliable surface loss data could be found in the literature. Therefore, a small surface loss probability of 0.01 was assumed, taken as half of that used for the reactive atomic F.

As shown in figure 2, an axially uniform magnetic field is applied in the direction parallel to the electrode surfaces. The electrode gap distance is 2 cm. Our approach of using a 1d3v PIC/MCC simulation follows previous work on such magnetized CCPs [39, 52, 54, 55, 79–81]. Magnetically induced drift motions of charged particles are included self-consistently, since all three velocity components are considered. However, interactions of charged particles with the lateral reactor walls are not included due to the 1d spatial resolution. Therefore, this approach assumes that the lateral reactor walls are located far

**Table 2.** Representative ion + $CF_4$ collision processes for various positive and negative ions considered in the model. For each ion species only ten reactions with the lowest energy thresholds, $\Delta E$, are shown. For each ion species, the first reaction corresponds to isotropic and the second reaction to anisotropic elastic scattering. The full lists of the ion + $CF_4$ molecule collision processes can be found in [66].

| # | Reaction | Products | $\Delta E$ |
|---|---|---|---|
| 1 | $CF_3^+ + CF_4 \rightarrow$ | $CF_3^+ + CF_4$ | 0 |
| 2 | | $CF_3^+ + CF_4$ | 0 |
| 3 | | $CF_3^+ + CF_3 + F$ | 5.621 |
| 4 | | $CF_2^+ + CF_4 + F$ | 5.843 |
| 5 | | $CF^+ + CF_4 + F_2$ | 7.546 |
| 6 | | $CF_3^+ + CF_2 + F_2$ | 7.598 |
| 7 | | $CF^+ + CF_4 + 2F$ | 9.146 |
| 8 | | $CF_3^+ + CF_2 + 2F$ | 9.198 |
| 9 | | $CF_2^+ + CF_3 + F_2$ | 9.864 |
| 10 | | $CF_2^+ + CF_3 + 2F$ | 11.464 |
| … | … | … | … |
| 1 | $CF_2^+ + CF_4 \rightarrow$ | $CF_2^+ + CF_4$ | 0 |
| 2 | | $CF_2^+ + CF_4$ | 0 |
| 3 | | $CF^+ + CF_4 + F$ | 3.303 |
| 4 | | $CF_2^+ + CF_3 + F$ | 5.621 |
| 5 | | $CF^+ + CF_3 + F_2$ | 7.324 |
| 6 | | $CF_2^+ + CF_2 + F_2$ | 7.598 |
| 7 | | $CF^+ + CF_3 + 2F$ | 8.924 |
| 8 | | $CF_2^+ + CF_2 + 2F$ | 9.198 |
| 9 | | $CF^+ + CF_2 + F_2 + F$ | 10.901 |
| 10 | | $CF^+ + CF_2 + 3F$ | 12.501 |
| … | … | … | … |
| 1 | $CF^+ + CF_4 \rightarrow$ | $CF^+ + CF_4$ | 0 |
| 2 | | $CF^+ + CF_4$ | 0 |
| 3 | | $CF^+ + CF_3 + F$ | 5.621 |
| 4 | | $CF^+ + CF_2 + F_2$ | 7.598 |
| 5 | | $CF^+ + CF_2 + 2F$ | 9.198 |
| 6 | | $CF^+ + CF + F_2 + F$ | 13.181 |
| 7 | | $CF^+ + CF + 3F$ | 14.781 |
| 8 | | $CF^+ + C + 2F_2$ | 17.192 |
| 9 | | $CF^+ + C + F_2 + 2F$ | 18.792 |
| 10 | | $CF^+ + C + 4F$ | 20.392 |
| … | … | … | … |
| 1 | $C^+ + CF_4 \rightarrow$ | $C^+ + CF_4$ | 0 |
| 2 | | $C^+ + CF_4$ | 0 |
| 3 | | $C^+ + CF_3 + F$ | 5.621 |
| 4 | | $C^+ + CF_2 + F_2$ | 7.598 |
| 5 | | $C^+ + CF_2 + 2F$ | 9.198 |
| 6 | | $C^+ + CF + F_2 + F$ | 13.181 |
| 7 | | $C^+ + CF + 3F$ | 14.781 |
| 8 | | $C^+ + C + 2F_2$ | 17.192 |
| 9 | | $C^+ + C + F_2 + 2F$ | 18.792 |
| 10 | | $C^+ + C + 4F$ | 20.392 |

(Continued.)

**Table 2.** (Continued.)

| # | Reaction | Products | $\Delta E$ |
|---|---|---|---|
| 1 | $F^+ + CF_4 \rightarrow$ | $F^+ + CF_4$ | 0 |
| 2 | | $F^+ + CF_4$ | 0 |
| 3 | | $F^+ + CF_3 + F$ | 5.621 |
| 4 | | $F^+ + CF_2 + F_2$ | 7.598 |
| 5 | | $F^+ + CF_2 + 2F$ | 9.198 |
| 6 | | $F^+ + CF + F_2 + F$ | 13.181 |
| 7 | | $F^+ + CF + 3F$ | 14.781 |
| 8 | | $F^+ + C + 2F_2$ | 17.192 |
| 9 | | $F^+ + C + F_2 + 2F$ | 18.792 |
| 10 | | $F^+ + C + 4F$ | 20.392 |
| 1 | $F^- + CF_4 \rightarrow$ | $F^- + CF_4$ | 0 |
| 2 | | $F^- + CF_4$ | 0 |
| 3 | | $CF_4 + F + e^-$ | 3.521 |
| 4 | | $F^- + CF_3 + F$ | 5.621 |
| 5 | | $CF_3 + F_2 + e^-$ | 7.542 |
| 6 | | $F^- + CF_2 + F_2$ | 7.598 |
| 7 | | $CF_3 + 2F + e^-$ | 9.142 |
| 8 | | $F^- + CF_2 + 2F$ | 9.198 |
| 9 | | $CF_2 + F_2 + F + e^-$ | 11.119 |
| 10 | | $CF_2 + 3F + e^-$ | 12.719 |
| … | … | … | … |
| 1 | $CF_3^- + CF_4 \rightarrow$ | $CF_3^- + CF_4$ | 0 |
| 2 | | $CF_3^- + CF_4$ | 0 |
| 3 | | $CF_3 + CF_4 + e^-$ | 1.871 |
| 4 | | $F^- + CF_2 + CF_4$ | 1.927 |
| 5 | | $CF_2 + CF_4 + F + e^-$ | 5.448 |
| 6 | | $CF_3^- + CF_3 + F$ | 5.621 |
| 7 | | $2CF_3 + F + e^-$ | 7.492 |
| 8 | | $F^- + CF + CF_4 + F$ | 7.510 |
| 9 | | $F^- + CF_2 + CF_3 + F$ | 7.548 |
| 10 | | $CF_3^- + CF_2 + F_2$ | 7.598 |
| … | … | … | … |

away from the electrodes so that such interactions can be neglected, which could otherwise be caused by magnetically induced particle drifts or by charged particles following the magnetic field lines. The top electrode ($x = L$) is grounded and the bottom electrode ($x = 0$) is driven by an RF voltage:

$$V(t) = V_0 \cos(2\pi f t), \tag{3}$$

where the voltage amplitude is $V_0 = 200\,\mathrm{V}$ and the frequency is $f = 13.56\,\mathrm{MHz}$. Elastic electron reflection and secondary electron emission induced by positive ions are considered in the simulations. A constant electron reflection coefficient of 0.7 and secondary electron emission coefficient of 0.07 are assumed. These values were found to yield good agreements with experimental results in previous studies [82]. A constant gas temperature of $T_{\mathrm{gas}} = 350\,\mathrm{K}$ is assumed in the simulations. In the simulations, between 500 and 5000 grid points and between 20 000 and 50 000 time steps per RF cycle were employed, depending on the discharge conditions, to fulfill the stability and accuracy requirements of the explicit electrostatic PIC/MCC scheme [83]. The simulations yield the time-averaged density profiles of all charged species and radicals, the generation rate of radicals, the electron energy probability function within different regions, as well as the spatiotemporal distributions of electron density, electric field, electron power absorption, ionization rate. The results presented in this work are obtained by averaging the simulation results over 1000 RF cycles after convergence.

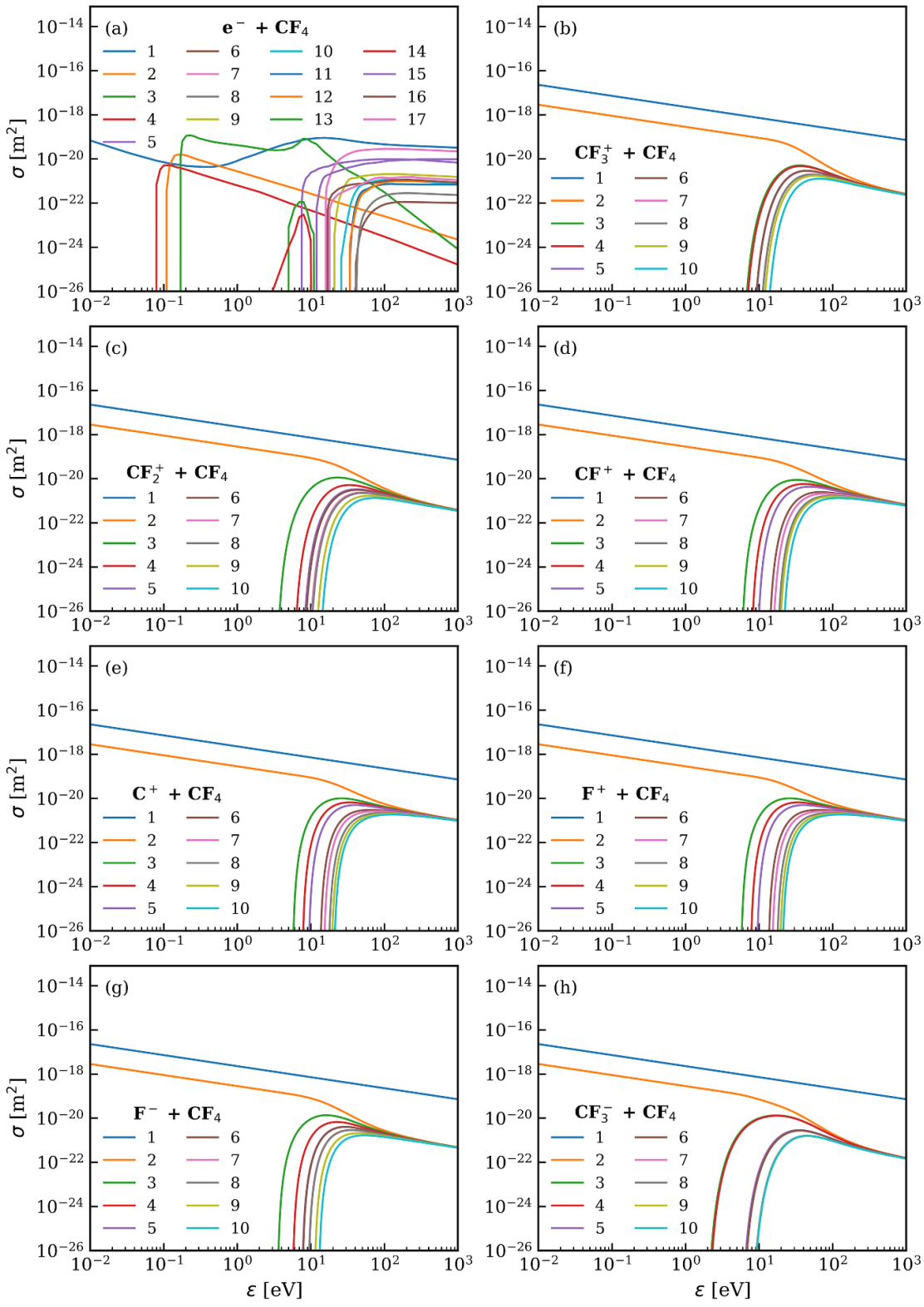



**Figure 1.** (a) Cross sections for $e^- + CF_4$ collisions (corresponding to table 1) and (b)–(h) representative ion + $CF_4$ collision processes for various positive and negative ions (corresponding to table 2) as a function of the kinetic energy. For ions, $\varepsilon$ denotes the kinetic energy in the center-of-mass frame.

## 3. Results

### 3.1. Magnetic field induced disruption of striations

In this section, the effects of an external magnetic field on a well established striation mode are studied. The simulations are conducted at a high pressure of 100 Pa, where striations are formed within the plasma bulk in the absence of a magnetic field, i.e. $B = 0$ G. In this case, a very low electron density is

**Table 3.** The values of the diffusion coefficient, $D_0$, for various radical species and $F_2$ at a reference pressure $p_0 = 1$ Pa and reference temperature $T_0 = 300$ K. These values are calculated as in [74].

| Species | $D_0$ ($m^2s^{-1}$) |
|---|---|
| $CF_3$ | 0.766 |
| $CF_2$ | 0.929 |
| CF | 1.212 |
| C | 2.18 |
| $F_2$ | 1.174 |
| F | 1.69 |

**Table 4.** Surface loss probabilities for $CF_4$ plasma radical species and $F_2$, including literature references and pre-set values.

| Species | $\alpha$ value | References |
|---|---|---|
| $CF_3$ | 0.2 | [76] |
| $CF_2$ | 0.23 | [76] |
| CF | 0.4 | [76] |
| C | 0.4 | [76] |
| $F_2$ | 0.01 | |
| F | 0.02 | [78] |

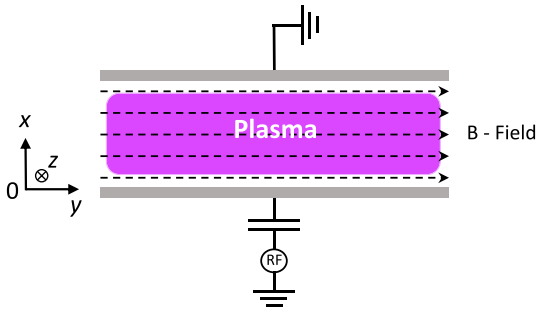



**Figure 2.** Schematic of a symmetric capacitive RF discharge with a transversal magnetic field.

present in the whole bulk region (see figures 3(a) and 4(a1)), which is much lower than the positive and negative ion densities and the space charges induced by the oscillations of the positive and negative ions in response to the RF bulk electric field cannot be compensated. However, when a uniform magnetic field of 130 G is applied, the striations at the center of the discharge gap start to be disrupted (see figure 3(b)), which is caused by an increased electron density. As shown in figures 4(b1)–(b4), due to the confinement of electrons by the B-field, both electron power absorption and ionization are enhanced in the plasma bulk. As described in [60], this is a consequence of the fact that the mobility of electrons in the direction perpendicular to the electrodes is reduced as a function of the externally applied magnetic field. For a fixed electron density, this leads to an enhanced bulk electric field and increased electron power absorption. This, in turn enhances the ionization and the electron density in the whole bulk region. The transport of electrons across the magnetic field lines, i.e. in the direction perpendicular to the electrodes, is induced by electron-neutral collisions, while they gyrate around the B-field lines. The electron density rises most prominently at the discharge center, since electrons gained high enough energy from being accelerated by the bulk electric field in this region and the newly generated low-energy electrons tend to remain locally confined by the applied magnetic field. As a result, the elevated electron density at the discharge center provides sufficient charge compensation for the space charges generated by the ion oscillations, which suppresses the development of striations.

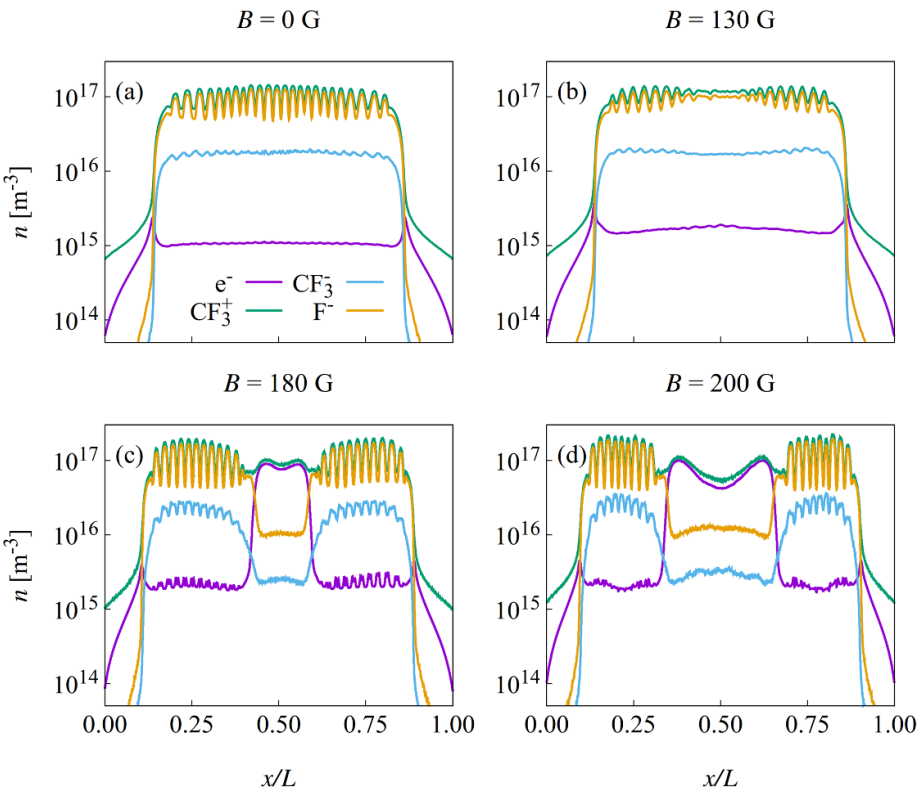



**Figure 3.** Time-averaged charged particle density profiles at magnetic fields of $B = 0, 130, 180$, and 200 G. The other discharge conditions are: $V_0 = 200$ V, $f = 13.56$ MHz, $p = 100$ Pa, $L = 2$ cm.

When the external magnetic field is increased to 180 G, an electron density peak, i.e. an electropositive core, is formed at the discharge center. The negative ion density becomes much lower than the electron density. Therefore, the ion–ion plasma is disrupted and striations can no longer form. The formation mechanism of this electropositive core is the same as that explained in [60]. This leads to the formation of a striation and m-DA hybrid mode.

When the magnetic field is further increased to 200 G, the electropositive core becomes even broader, while the striation region further shrinks. As shown in figures 4(d1)–(d4), this is because an even stronger electric field develops in the striation region, leading to more intense electron power absorption and enhanced ionization. Therefore, more low-energy electrons are generated and subsequently confined by the magnetic field near the discharge center, resulting in a broader electropositive core. However, since the ionization peaks are located at the edges of the electropositive core region and few electrons are created in the discharge center, the electron density decays slightly from this edge towards the discharge center. In this case, a weak drift electric field builds up at the center due to the lower local electron density and plasma conductivity. In addition, it should be noted that although the formation of striations is primarily driven by the oscillations of $CF_3^+$ and $F^-$ ions, which generate space charges and induce a strong internal electric field, comb-like structures also become pronounced in the density profiles of $CF_3^-$ ions and electrons in the cases of 180 G and 200 G, as shown in figures 3(c) and (d). This is because the striated electric field gets much stronger under these high magnetic field conditions.

These substantial changes in the operation mode and electron power absorption dynamics also influence process relevant plasma properties significantly. Figures 5(a) and (b) show the time-averaged F atom density profile and spatial distribution of the F source rate at magnetic fields of $B = 0, 130, 180$, and 200 G, respectively. While the F atom density increases only slightly, when an external magnetic field of 130 G is applied, it rises substantially when the magnetic field is increased to 180 G and 200 G. The dominant processes leading to the production of F atoms are dissociative ionization (e.g. processes 7 and 9 in table 1), dissociative attachment (process 14 in table 1), and neutral dissociation (processes 15–17 in table 1). As shown in figure 5(b), under these high magnetic field conditions, F atom production is strongly enhanced within the striation region due to the intensified electric field and electron power absorption. This leads to a significantly higher overall F atom density, despite the very low generation rate near the discharge center where few high-energy electrons are present.

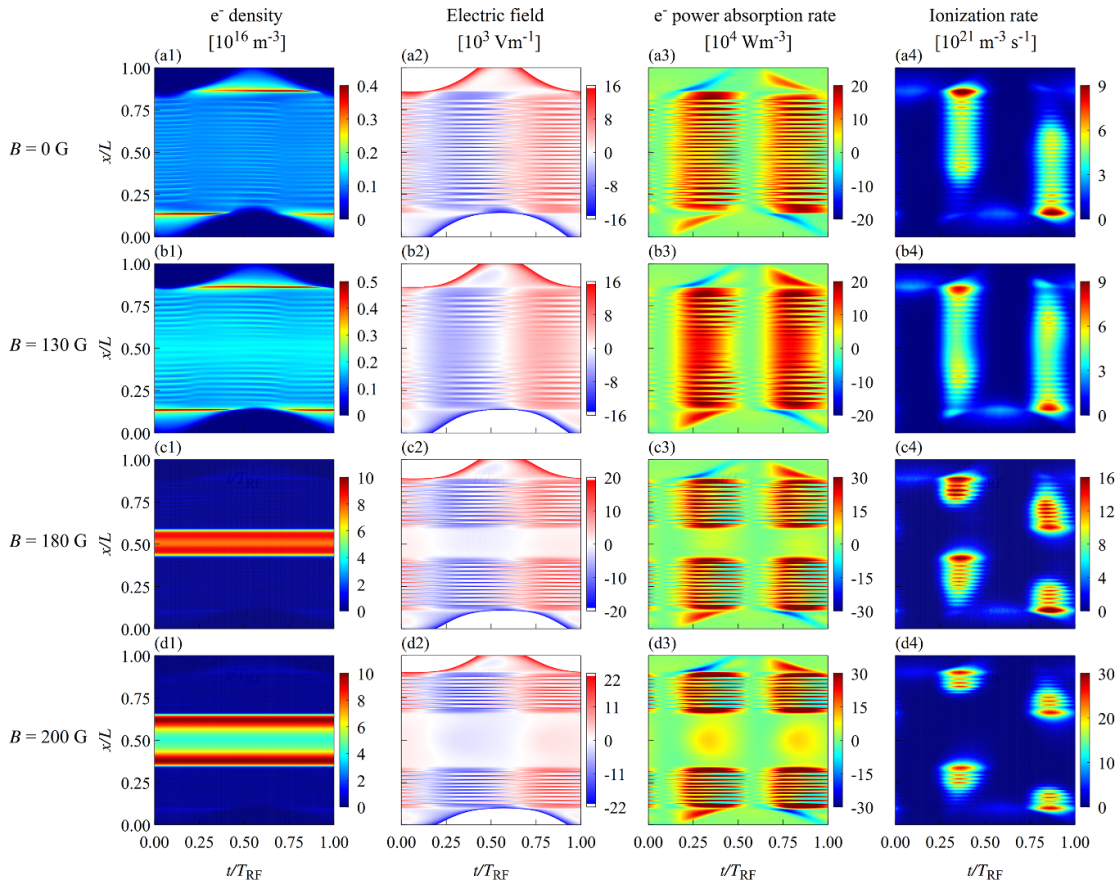



**Figure 4.** Spatio-temporal plots of the electron density (first column), electric field (second column), electron power absorption rate (third column), and ionization rate (fourth column) at magnetic fields of $B = 0, 130, 180$, and 200 G. The other discharge conditions are the same as in figure 3.

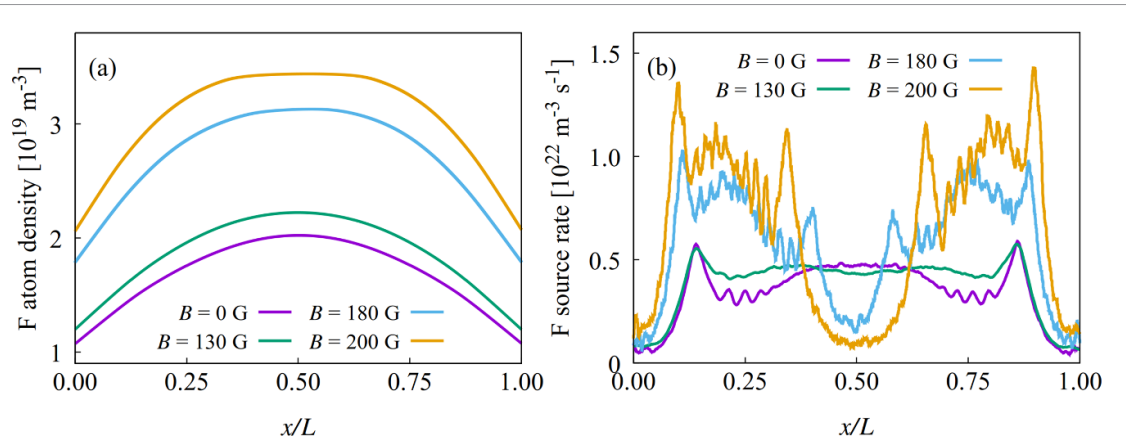



**Figure 5.** (a) Time-averaged F atom density profiles and (b) spatial distributions of the F atom generation rate at magnetic fields of $B = 0, 130, 180$, and 200 G. The other discharge conditions are the same as in figure 3.

The time averaged electron energy probability functions (EEPFs) close to the discharge center in the cases of different magnetic fields are shown in figure 6(a). At 0 and 130 G, the drift electric field at the discharge center remains strong, resulting in a pronounced high-energy tail of the EEPF. In contrast, at 180 G and 200 G, the formation of an electropositive core significantly attenuates the local electric field. Consequently, the high-energy tail of the EEPF is largely depleted in the discharge center, while the population of low-energy electrons increases. Most of the electrons cannot reach the energy threshold for ionization in the center. Figure 6(b) shows the EEPFs close to $x/L = 0.25$, i.e. in the edge region of the

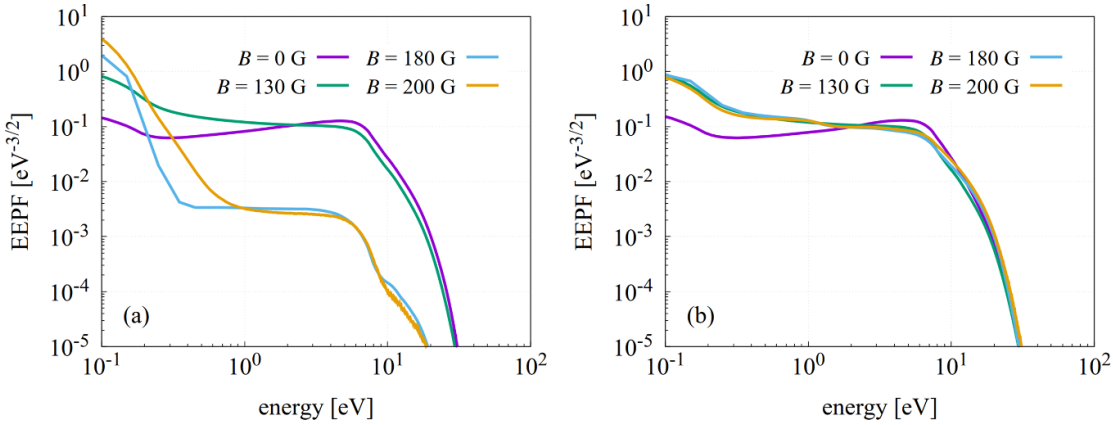



**Figure 6.** Time-averaged electron energy probability functions (EEPFs) (a) close to the discharge center (the results are averaged over $0.45 < x/L < 0.55$) and (b) close to $x/L = 0.25$ (the results are averaged over $0.2 < x/L < 0.3$) at magnetic fields of $B =$ 0, 130, 180, and 200 G. The other discharge conditions are the same as in figure 3.

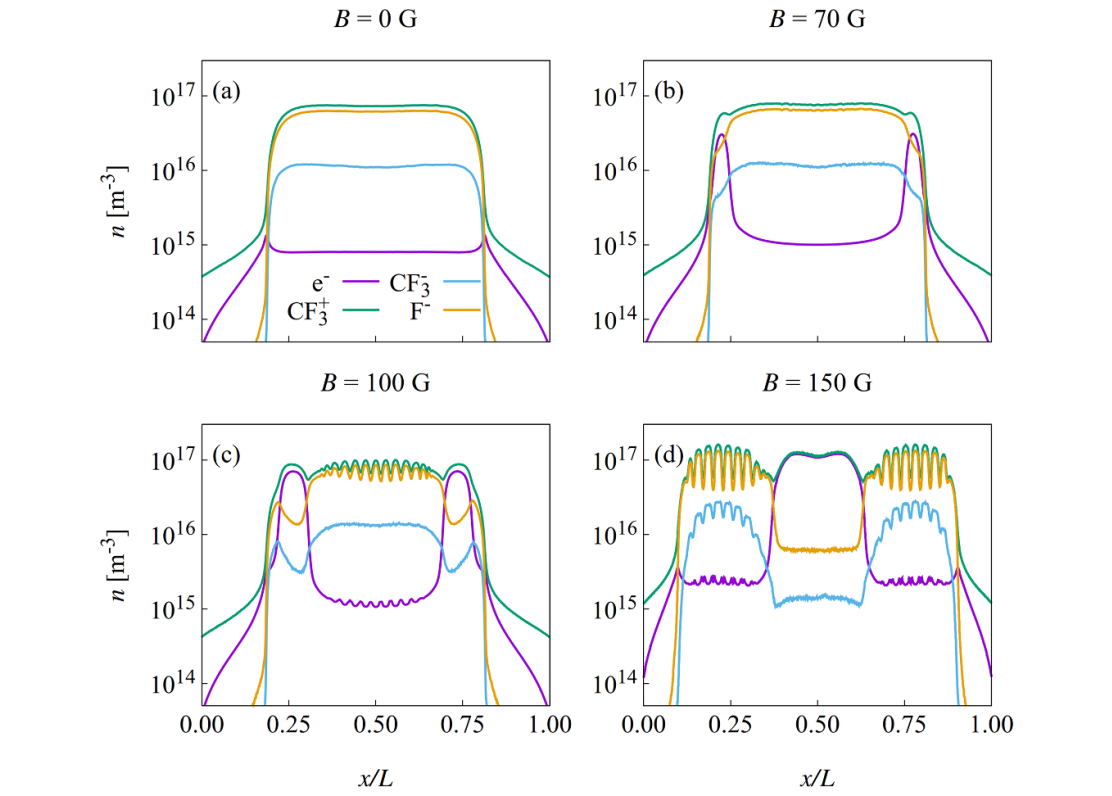



**Figure 7.** Time-averaged charged particle density profiles at magnetic fields of $B = 0, 70, 100$, and 150 G. The other discharge conditions are $V_0 = 200$ V, $f = 13.56$ MHz, $p = 50$ Pa, $L = 2$ cm.

plasma bulk close to the sheath, where striations are formed in all the cases. Although electron power absorption is strongly enhanced at this location for magnetic fields of 180 G and 200 G, this does not result in a more pronounced high-energy tail in the EEPF. This is because strong magnetic confinement increases the residence time of electrons in the high-field region. As a result, electrons undergo a larger number of collisions and dissipate their absorbed energy more efficiently through collisional processes.

### 3.2. Magnetic field induced formation of striations

In the following, we discuss the effects of an external magnetic field on the discharge in the case where the positive and negative ion densities are around the critical ion density required for the formation of striations, but striations do not occur in the absence of a magnetic field. The pressure is reduced

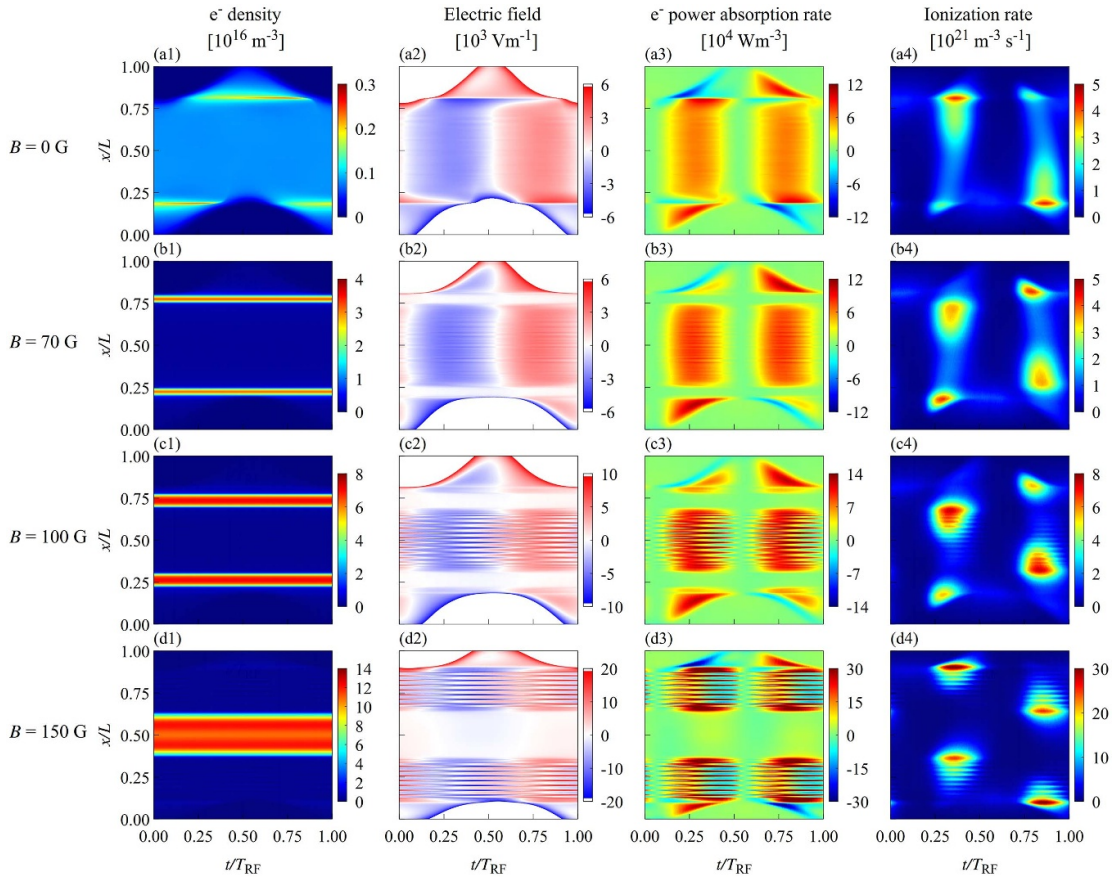



**Figure 8.** Spatio-temporal plots of the electron density (first column), electric field (second column), electron heating rate (third column), and ionization rate (fourth column) at magnetic fields of $B = 0, 70, 100$, and 150 G. The other discharge conditions are the same as in figure 7.

to 50 Pa, while all other discharge conditions remain unchanged. As shown in figure 7(a), when no magnetic field is applied, although the densities of the main positive and negative ions, i.e. $CF_3^+$ and $F^-$, exceed the threshold value for striation formation, which is $6.2 \times 10^{16}$ m$^{-3}$ based on the ion–ion plasma model [31], the discharge still operates in the DA mode and no striations appear. This is because the ion–ion model from which the critical ion density is derived neglects the role of electrons. When the electron density is relatively high, the space charge induced by the ion oscillations can be effectively compensated by electrons, preventing the formation of striations. This is also the case when a weak magnetic field, e.g. 70 G, is applied. As shown in figure 7(b), although the $CF_3^+$ and $F^-$ densities increase slightly in the plasma bulk, the electron density also rises, and striations still cannot be formed. However, in this case, electron density peaks appear near the edges of the bulk region and the discharge operates in the m-DA mode. A similar phenomenon was observed in our previous study [60]. Unlike the situation shown in figure 3(c), where an electron density peak forms at the discharge center, the drift electric field in the plasma bulk in this case is sufficient to accelerate some electrons to the ionization threshold. Nevertheless, the ionization rate remains too low to produce enough low-energy electrons to form an electron density peak at the discharge center. Instead, electrons cause significant ionization only after they traversed nearly the entire bulk region and reached the edges of the collapsing sheaths, as shown in figure 7(b4). The newly generated low-energy electrons are then locally confined by the magnetic field, resulting in electron density peaks at the edges of the plasma bulk.

When the magnetic field is increased to 100 G, the ion densities rise. The oscillatory motion of the ions generates enhanced space charges that can no longer be compensated by the electrons. As a result, striations are formed in the center of the plasma bulk, as shown in figures 7(c) and 8(c1)–(c4). In addition, the electron density peaks at the edges of the plasma bulk are further enhanced due to the higher electron power absorption in the bulk region and the more intensive ionization occurring near the collapsing sheath edges. Consequently, a striation and m-DA hybrid mode is established with striations being in the center and electropositive regions located at the edges of the plasma bulk. When

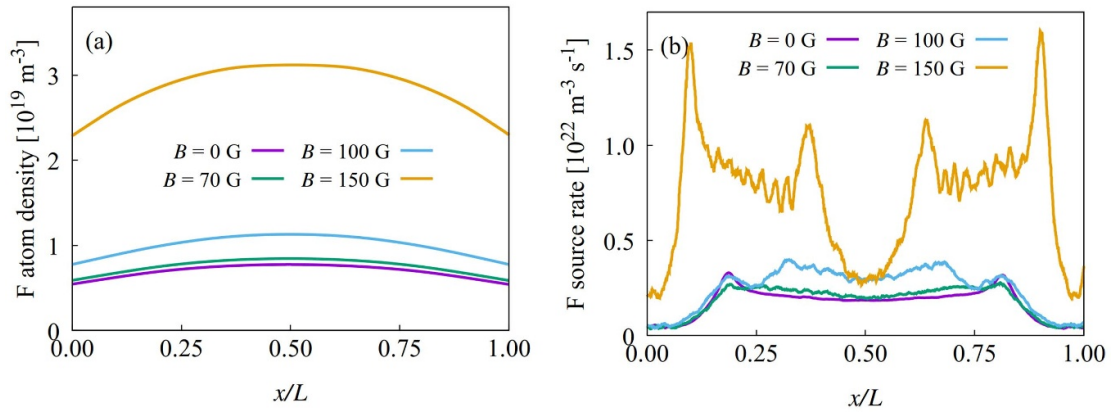



**Figure 9.** (a) Time-averaged F atom density profiles and (b) spatial distributions of the F atom generation rate at magnetic fields of $B = 0, 70, 100$, and 150 G. The other discharge conditions are the same as in figure 7.

the magnetic field is further increased to 150 G, the electric field is significantly enhanced due to the reduced cross-field conductivity, which further enhances the electron power absorption (see figures 8(d2) and (d3)). As a result, a large number of electrons gain sufficient energy for ionization before reaching the discharge center. In addition to that, the longer residence time of the electrons caused by the cross-field motion contributes to a significantly higher ionization rate. As shown in figure 8(d4), strong ionization peaks are formed near the discharge center in both the first and second halves of the RF cycle. The newly generated low-energy electrons are confined at the discharge center by the magnetic field, resulting in a broad electropositive core. Highly electronegative zones and striations are formed at the edges of the plasma bulk. We note that, although the electric field is partially reversed in each half of the RF period at different spatial locations due to the striated structure, the amplitude of the reversed electric field is much lower than the fraction of the striated field that points in the opposite direction and does not lead to significant power loss, as shown in figure 8(d3). It is also noted that, in the 70 G and 100 G cases, the high electron densities near the sheath edges result in evident ionization during sheath expansion. In contrast, for the 150 G case, ionization during sheath expansion is much less pronounced than in the bulk region, owing to the substantially lower electron density at the sheath edges in this case.

Figures 9(a) and (b) show the time-averaged F atom density profiles and the F atom generation rates at different magnetic fields, respectively. Although the discharge mode transitions from the DA mode to the m-DA mode and subsequently to the hybrid m-DA/striation mode as the magnetic field increases from 0 G to 70 G and 100 G, both the F atom density and the F atom generation rate exhibit only a slight increase. In contrast, at 150 G, despite the very low F atom generation rate at the discharge center caused by the formation of the electropositive core, the enhanced electron power absorption in the striation region leads to a substantially higher F atom generation, ultimately resulting in a significantly increased overall F atom density. The time-averaged EEPFs at the discharge center for different magnetic fields are shown in figure 10(a). As the magnetic field increases from 0 G to 70 G and 100 G, the high-energy tail of the EEPF remains nearly unchanged, whereas its values in the mid-energy range (2–10 eV) decrease slightly and the low-energy electron population increases. This behavior arises because the external magnetic field enhances the gyromotion of electrons around the magnetic field lines. While the magnetic field does not change the electron–neutral collision frequency for a given electron energy, it increases the effective path length and residence time of electrons within the reactor. As a result, electrons experience a larger number of collisions during their transport between the electrodes, leading to more efficient energy loss. A similar trend is observed for the EEPF at 150 G near $x/L = 0.25$, as shown in figure 10(b). In the EEPF at 150 G at the discharge center, as well as in those at 70 G and 100 G in the edge region of the bulk near $x = 0.25$, the high-energy tail becomes depleted due to the substantial reduction of the electric field within the electropositive region.

Overall, these results show that although the ion dynamics is hardly affected directly by an external magnetic field of several tens to hundreds of Gauss, discharges operated in or near the striation regime can be strongly influenced by the magnetic field through its impact on the electron dynamics. This effect is often accompanied by the formation of an electropositive core, leading to a striation and m-DA hybrid mode. More importantly, the magnetic field can significantly enhance the electron power absorption within the striated electric field and consequently increase the generation and density of radicals. In addition, striations are neither strictly beneficial nor detrimental for radical production, as

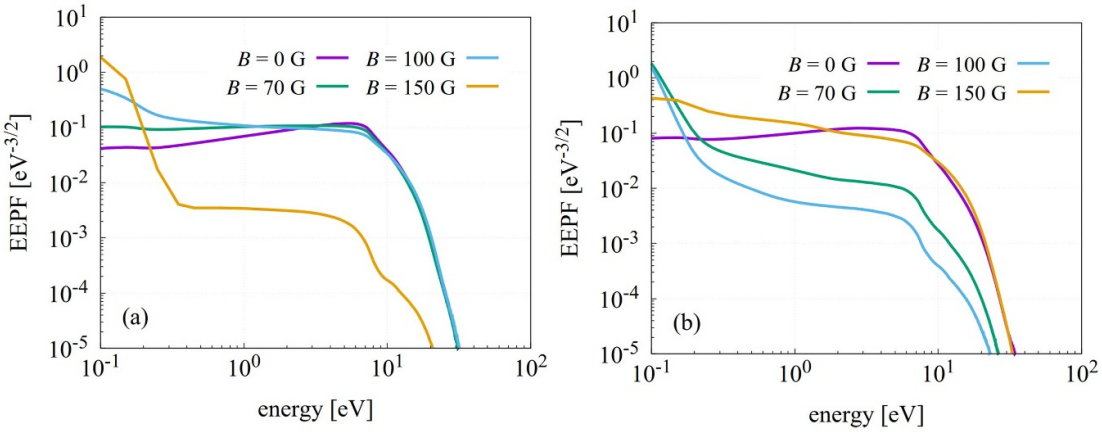



**Figure 10.** Time-averaged electron energy probability functions (EEPF) (a) close to the discharge center (the results are averaged over $0.45 < x/L < 0.55$ and (b) close to $x/L = 0.25$ (the results are averaged over $0.2 < x/L < 0.3$) at magnetic fields of $B =$ 0, 70, 100, and 150 G. The other discharge conditions are the same as in figure 7.

their impact mainly depends on how electron power absorption is redistributed spatially by the magnetic field. Although the partial suppression of existing striations at high pressure conditions reduces radical generation locally, radical production can be enhanced in the remaining striated regions, leading to an overall increase in radical density at high magnetic fields. These effects are highly relevant for plasma etching and deposition processes.

## 4. Conclusions

In this work, we investigated the effects of an external homogeneous magnetic field on capacitively coupled $CF_4$ RF plasmas operated in and close to the striation regime using a 1d3v PIC/MCC model. The results show that, although the ions remain essentially unmagnetized under the relatively weak magnetic fields considered here, striations can either be suppressed or induced through the influence of the magnetic field on the electron dynamics depending on the discharge conditions.

When a magnetic field of 130 G is applied to an otherwise well established striation mode at 100 Pa and B = 0 G, where a strong electronegativity is present throughout the plasma bulk, the electron density at the discharge center increases slightly due to the enhanced electron power absorption within the striated electric field. In this case, the electrons are able to compensate the space charge generated by the ion oscillations and the striations are consequently disrupted. When the magnetic field is further increased to 180 G and 200 G, an electron density peak, i.e. an electropositive core, forms at the discharge center. Under these conditions, the ion–ion plasma can no longer be sustained, and striations cannot be formed.

At a lower pressure condition of 50 Pa, where the discharge operates close to the striation regime, although the positive and negative ion densities exceed the threshold value, no striations are formed in the absence of a magnetic field because the relatively high electron density in the plasma bulk effectively compensates the space charge arising from ion oscillations. As a result, the discharge remains in the DA mode. When a weak magnetic field, i.e. 70 G, is applied, both the ion and electron densities increase slightly in the bulk region, while still no striations are formed. However, local electron density peaks develop near the edges of the plasma bulk and the discharge operates under the m-DA mode. By increasing the magnetic field to 100 G, the ion densities grow further and the space charge generated by their oscillations can no longer be fully compensated by the electrons. Striations consequently emerge in the central region of the plasma bulk, while enhanced ionization near the sheath edges further amplifies the electron density peaks in those regions. This results in the formation of a hybrid striation and m-DA mode. When the magnetic field is raised to 150 G, the electric field in the bulk becomes significantly stronger, leading to enhanced electron power absorption and strong ionization peaks close to the center. A broad electropositive core is formed at the center region while high electronegativity and striations are present at the edges of the plasma bulk.

Accompanied by the changes in the operation mode, the magnetic field also strongly modulates the generation of radicals. In both the 100 Pa and 50 Pa cases, when a strong magnetic field ($B \geqslant 150$ G) is

applied, the electric field and the electron power absorption within the striation region are significantly enhanced. This, in turn, substantially increases the F atom generation rate and the overall F atom density despite the low F atom production within the electropositive core region.

These findings demonstrate that the externally applied magnetic fields can serve as an effective control parameter to tailor plasma operation modes and reactive species production in electronegative CCPs. We expect these findings to provide valuable insights for optimizing plasma etching and deposition processes, in which precise control of ion and radical densities is crucial for achieving high-performance material processing.

## Acknowledgments

This work was supported by the German Research Foundation in the frame of the Project 'Electron heating in reactive and magnetized capacitive RF plasmas: From fundamental understanding to knowledge based process control' (No. 428942393) and by the National Natural Science Foundation of China (No. 12020101005, 12475202). AD received support from the J Bolyai Scholarship of the Hungarian Academy of Sciences. The authors gratefully acknowledge Dr Kazuki Denpoh for providing the complete set of ion-$CF_4$ molecule reaction processes from his work "Studies on $CF_4$ Plasmas Using Particle-Based Simulation Models".

## Data availability statement

The data that support the findings of this study are openly available at the following URL/DOI: https://rdpcidat.rub.de [84]. Data will be available from 01 May 2026.

## ORCID iDs

Li Wang 0000-0002-3106-2779
Aranka Derzsi 0000-0002-8005-5348
Peter Hartmann 0000-0003-3572-1310
Zoltán Donkó 0000-0003-1369-6150
Maximilian Ryppa 0009-0008-8649-6524
Constantin Neuroth 0009-0006-0775-1407
Florian Beckfeld 0000-0001-8605-2634
Wan Dong 0000-0002-0724-1697
Yuan-Hong Song 0000-0001-5712-9241
Julian Schulze 0000-0001-7929-5734

## References

[1] Lieberman M A and Lichtenberg A J 2005 *Principles of Plasma Discharges and Materials Processing* 2nd edn (Wiley)
[2] Chabert P and Braithwaite N 2011 *Physics of Radio-Frequency Plasmas* (Cambridge University Press)
[3] Adamovich I *et al* 2022 *J. Phys. D: Appl. Phys.* **55** 373001
[4] Rauf S and Balakrishna A 2017 *J. Vac. Sci. Technol. A* **35** 021308
[5] Lafleur T, Delattre P A, Johnson E V and Booth J P 2012 *Appl. Phys. Lett.* **101** 124104
[6] Zhang Y, Kushner M J, Moore N, Pribyl P and Gekelman W 2013 *J. Vac. Sci. Technol. A* **31** 061311
[7] Donkó Z, Schulze J, Hartmann P, Korolov I, Czarnetzki U and Schüngel E 2010 *Appl. Phys. Lett.* **97** 081501
[8] Gudmundsson J T and Ventéjou B 2015 *J. Appl. Phys.* **118** 153302
[9] Wang L, Wen D Q, Tian C B, Song Y H and Wang Y N 2021 *Acta Phys. Sin.* **70** 095214
[10] Lafleur T, Boswell R W and Booth J P 2012 *Appl. Phys. Lett.* **100** 194101
[11] Fu Y, Zheng B, Wen D Q, Zhang P, Fan Q H and Verboncoeur J P 2020 *Plasma Sources Sci. Technol.* **29** 09LT01
[12] Wen D Q, Kawamura E, Lieberman M A, Lichtenberg A J and Wang Y N 2016 *Plasma Sources Sci. Technol.* **26** 015007
[13] Schulze J, Donkó Z, Heil B G, Luggenhölscher D, Mussenbrock T, Brinkmann R P and Czarnetzki U 2008 *J. Phys. D: Appl. Phys.* **41** 105214
[14] Derzsi A, Bruneau B, Gibson A R, Johnson E, O'Connell D, Gans T, Booth J P and Donkó Z 2017 *Plasma Sources Sci. Technol.* **26** 034002
[15] Rauf S, Bera K and Collins K 2009 *Plasma Sources Sci. Technol.* **19** 015014
[16] Belenguer P and Boeuf J P 1990 *Phys. Rev. A* **41** 4447–59
[17] Turner M M 1995 *Phys. Rev. Lett.* **75** 1312–5
[18] Surendra M and Dalvie M 1993 *Phys. Rev. E* **48** 3914–24

[19] Schulze J, Donko Z, Derzsi A, Korolov I and Schuengel E 2015 *Plasma Sourc. Sci. Technol.* **24** 015019
[20] Godyak V A and Khanneh A S 1986 *IEEE Trans. Plasma Sci.* **14** 112–23
[21] Daksha M, Derzsi A, Wilczek S, Trieschmann J, Mussenbrock T, Awakowicz P, Donkó Z and Schulze J 2017 *Plasma Sources Sci. Technol.* **26** 085006
[22] Schulze J, Derzsi A, Dittmann K, Hemke T, Meichsner J and Donkó Z 2011 *Phys. Rev. Lett.* **107** 275001
[23] Liu G H, Liu Y X, Wen D Q and Wang Y N 2015 *Plasma Sources Sci. Technol.* **24** 034006
[24] Proshina O V, Rakhimova T V, Rakhimov A T and Voloshin D G 2010 *Plasma Sources Sci. Technol.* **19** 065013
[25] Dittmann K, Matyash K, Nemschokmichal S, Meichsner J and Schneider R 2010 *Contrib. Plasma Phys.* **50** 942–53
[26] Tian C B, Wang L, Vass M, Wang X K, Dong W, Song Y H, Wang Y N and Schulze J 2024 *Plasma Sources Sci. Technol.* **33** 075008
[27] Liu Y X, Schüngel E, Korolov I, Donkó Z, Wang Y N and Schulze J 2016 *Phys. Rev. Lett.* **116** 255002
[28] Wang L, Wen D Q, Zhang Q Z, Song Y H, Zhang Y R and Wang Y N 2019 *Plasma Sources Sci. Technol.* **28** 055007
[29] Mahdavipour B and Gudmundsson J T 2025 *Plasma Sources Sci. Technol.* **34** 045005
[30] Zhou Z, Wang X, Li H, Yang D, Zhang W, Schulze J, Hartmann P, Donkó Z, Liu Y and Fu Y 2025 *Plasma Sources Sci. Technol.* **34** 085014
[31] Liu Y X, Korolov I, Schüngel E, Wang Y N, Donkó Z and Schulze J 2017 *Plasma Sources Sci. Technol.* **26** 055024
[32] Masheyeva R, Vass M, Wang X K, Liu Y X, Derzsi A, Hartmann P, Schulze J and Donkó Z 2024 *Plasma Sources Sci. Technol.* **33** 045019
[33] Liu Y X, Korolov I, Schüngel E, Wang Y N, Donkó Z and Schulze J 2017 *Phys. Plasmas* **24** 073512
[34] Wang X K, Liu Y X, Wang X Y, Zhang Q Z, Zhao K and Wang Y N 2021 *Plasma Sources Sci. Technol.* **30** 055019
[35] Liu Y X, Donkó Z, Korolov I, Schüngel E, Wang Y N and Schulze J 2019 *Plasma Sources Sci. Technol.* **28** 075005
[36] Lieberman M A, Lichtenberg A J and Savas S E 1991 *IEEE Trans. Plasma Sci.* **19** 189–96
[37] You S J, C W Chung, Bai K H and Chang H Y 2002 *Appl. Phys. Lett.* **81** 2529–31
[38] Kushner M J 2003 *J. Appl. Phys.* **94** 1436–47
[39] Yang S, Zhang Y, Wang H Y, Wang S and Jiang W 2017 *Phys. Plasmas* **24** 033504
[40] Eremin D *et al* 2023 *Plasma Sources Sci. Technol.* **32** 045007
[41] Eremin D *et al* 2023 *Plasma Sources Sci. Technol.* **32** 045008
[42] Berger B, Eremin D, Oberberg M, Engel D, Wölfel C, Zhang Q Z, Awakowicz P, Lunze J, Brinkmann R P and Schulze J 2023 *Plasma Sources Sci. Technol.* **32** 045009
[43] Yeom G Y, Thornton J A and Kushner M J 1989 *J. Appl. Phys.* **65** 3825–32
[44] Bera K, Rauf S, Kenney J, Dorf L and Collins K 2010 *J. Appl. Phys.* **107** 053302
[45] Lee S H, You S J, Chang H Y and Lee J K 2007 *J. Vac. Sci. Technol. A* **25** 455–63
[46] Guo Y Q, Sun J Y, Zhang Q Z, Ma F F, Liu X M and Wang Y N 2021 *Plasma Proc. Polym.* **18** e2100072
[47] Wang L, Vass M, Donkó Z, Hartmann P, Derzsi A, Song Y H and Schulze J 2021 *Plasma Sources Sci. Technol.* **30** 10LT01
[48] Zhang Q Z, Sun J Y, Lu W Q, Schulze J, Guo Y Q and Wang Y N 2021 *Phys. Rev. E* **104** 045209
[49] Patil S, Sharma S, Sengupta S, Sen A and Kaganovich I 2022 *Phys. Rev. Res.* **4** 013059
[50] Yao J, Liu C, He F, Miao J, Ouyang J and Zheng B 2024 *Plasma Sources Sci. Technol.* **33** 105010
[51] Turner M M, Hutchinson D A W, Doyle R A and Hopkins M B 1996 *Phys. Rev. Lett.* **76** 2069–72
[52] Wang L, Wen D Q, Hartmann P, Donkó Z, Derzsi A, Wang X F, Song Y H, Wang Y N and Schulze J 2020 *Plasma Sources Sci. Technol.* **29** 105004
[53] Liu J R, Wang X K, Wang L, Zhao K, Liu Y X, Song Y H and Wang Y N 2024 *Plasma Process. Polym.* **21** e2300219
[54] Yang S, Zhang Y, Wang H, Cui J and Jiang W 2017 *Plasma Process. Polym.* **14** 1700087
[55] Yang S, Chang L, Zhang Y and Jiang W 2018 *Plasma Sources Sci. Technol.* **27** 035008
[56] Trieschmann J, Shihab M, Szeremley D, Elgendy A E, Gallian S, Eremin D, Brinkmann R P and Mussenbrock T 2013 *J. Phys. D: Appl. Phys.* **46** 084016
[57] Oberberg M, Kallähn J, Awakowicz P and Schulze J 2018 *Plasma Sources Sci. Technol.* **27** 105018
[58] Oberberg M, Berger B, Buschheuer M, Engel D, Wölfel C, Eremin D, Lunze J, Brinkmann R P, Awakowicz P and Schulze J 2020 *Plasma Sources Sci. Technol.* **29** 075013
[59] Sun J Y, Zhang Q Z, Liu J R, Song Y H and Wang Y N 2020 *Plasma Sources Sci. Technol.* **29** 114002
[60] Wang L, Vass M, Donkó Z, Hartmann P, Derzsi A, Song Y H and Schulze J 2022 *Plasma Sources Sci. Technol.* **31** 06LT01
[61] Kurihara M, Petrovic Z L and Makabe T 2000 *J. Phys. D: Appl. Phys.* **33** 2146
[62] Derzsi A, Hartmann P, Vass M, Horváth B, Gyulai M, Korolov I, Schulze J and Donkó Z 2022 *Plasma Sources Sci. Technol.* **31** 085009
[63] Brandt S *et al* 2016 *Plasma Sources Sci. Technol.* **25** 045015
[64] Bonham R A 1994 *Jpn. J. Appl. Phys.* **33** 4157
[65] Denpoh K and Nanbu K 1998 *J. Vac. Sci. Technol.* **16** 1201–6
[66] Denpoh K 1998 Studies on CF4 plasmas using particle-based simulation models *Doctor Thesis* Department of Mechanical Engineering, Graduate School of Tohoku University
[67] Georgieva V and Bogaerts A 2005 *J. Appl. Phys.* **98** 023308
[68] Denpoh K and Nanbu K 2022 *J. Vac. Sci. Technol. A* **40** 063007
[69] Georgieva V, Bogaerts A and Gijbels R 2003 *J. Appl. Phys.* **93** 2369–79
[70] Rauf S and Kushner M J 1997 *J. Appl. Phys.* **82** 2805–13
[71] Denpoh K and Nanbu K 2000 *Jpn. J. Appl. Phys.* **39** 2804
[72] Chapman S and Cowling T G 1939 *Mathematical Theory of Non-Uniform Gases* (Cambridge University Press)
[73] Winn E B 1950 *Phys. Rev.* **80** 1024–7
[74] Cussler E L 2009 *Diffusion: Mass Transfer in Fluid Systems* (Cambridge University Press)
[75] Hash D B, Bose D, Rao M V V S, Cruden B A, Meyyappan M and Sharma S P 2001 *J. Appl. Phys.* **90** 2148–57
[76] Toneli D, Pessoa R, Roberto M and Gudmundsson J T 2019 *Plasma Sources Sci. Technol.* **28** 025007
[77] Kota G P, Coburn J W and Graves D B 1999 *J. Vac. Sci. Technol. A* **17** 282–90
[78] Gudmundsson J 2002 *J. Phys. D: Appl. Phys.* **35** 328
[79] Yang S, Zhang Y, Wang H Y, Wang S and Jiang W 2017 *Plasma Sources Sci. Technol.* **26** 065011

[80] Yang S, Innocenti M E, Zhang Y, Yi L and Jiang W 2017 *J. Vac. Sci. Technol. A* **35** 061311
[81] Sharma S, Kaganovich I D, Khrabrov A V, Kaw P and Sen A 2018 *Phys. Plasmas* **25** 080704
[82] Wang X K, Korolov I, Wilczek S, Masheyeva R, Liu Y X, Song Y H, Hartmann P, Donkó Z and Schulze J 2024 *Plasma Sources Sci. Technol.* **33** 085001
[83] Vahedi V and Surendra M 1995 *Comput. Phys. Commun.* **87** 179–98
[84] Wang L, Derzsi A, Hartmann P, Donkó Z, Ryppa M A, Neuroth C, Beckfeld F, Dong W, Song Y H and Schulze J 2026 Magnetically induced formation and disruption of striations in capacitively coupled radio-frequency CF4 plasmas *Research data repository of the RUB Research Department Plasmas with Complex Interactions* (available at: https://rdpcidat.rub.de)